Intrinsic and complex defect engineering of quasi-one-dimensional ribbons math xmlns="http://www.w3.org/1998/Math/MathML">mrow>msub>mi>Sb/mi>mn>2/mn>/msub>msub>mi mathvariant="normal">S/mi>mn>3/mn>/msub>/mrow>/math> for photovoltaics performance

Rumeng Zhao, Xiuli Yang, Hongliang Shi, and Mao-Hua Du

Phys. Rev. Materials **5**, 054605 — Published 12 May 2021

DOI: 10.1103/PhysRevMaterials.5.054605

Intrinsic and complex defect engineering of quasi-one-dimensional ribbons Sb_2S_3 for photovoltaics performance

Rumeng Zhao[1], Xiuli Yang[1], Hongliang Shi[1,*] and Mao-Hua Du[2,*]

[1]Department of Physics, Beihang University, Beijing 100191, China

[2]Materials Science and Technology Division, Oak Ridge National Laboratory, Oak Ridge, TN 37831, USA

Keywords: Sb_2S_3, point defects, defect complexes, photovoltaics, DFT calculation

*Corresponding Author: Hongliang Shi (hlshi@buaa.edu.cn), Mao-Hua Du (mhdu@ornl.gov)

Abstract

Sb_2S_3 has attracted great attention recently as a prospective solar cell absorber material. In this work, intrinsic defects, dopants, and their complexes in Sb_2S_3 are systematically investigated by using hybrid functional theory. V_{Sb} and V_S are dominant native defects and pin the Fermi level near the midgap, which is consistent with the high resistivity observed experimentally. Both V_{Sb} and V_S introduce deep levels inside band gap, which can trap free carriers. Our calculated deep transition levels of V_{Sb} and Sb_S are consistent well with the results of the deep level transient spectroscopy measurement. We further study dopants (including Cu, Ti, Zn, Br and Cl) in Sb_2S_3 and find that Zn and Br/Cl are shallow acceptors and donors, respectively, which may be used to control the carrier and trap densities in Sb_2S_3. In addition, the defect complexes, *i.e.*, $Cu(Zn)_{Sb}$+V_S and $Cl(Br)_S$+V_{Sb} are also investigated. The interaction between the donor and acceptor defects makes the defect levels of complexes shallower and less detrimental to carrier transport.

I. Introduction

High-efficiency, earth-abundant and non-toxic solar materials are indispensable in photovoltaics (PV) technologies. In the last few decades, solar cell absorber materials such as silicon [1], CdTe [2], $Cu(In,Ga)Se_2$ (CIGS) [3, 4] and organic-inorganic hybrid perovskites (e.g., $CH_3NH_3PbI_3$) [5] have drawn extensive attentions because of their impressive certified efficiencies. However, there are still some inevitable shortcomings that limit their performance as solar cell materials. For example, silicon has poor optical absorption; thus, large crystals are required in a Si solar cell [6, 7]. For second-generation solar cells, CdTe contains toxic heavy metals and suffers from a relatively low open circuit voltage (V_{OC}) [8] while CIGS has complex defect problems that appear to limit any significant improvements in cell efficiency [9]. For the hybrid organic-inorganic lead halide perovskites, their air and thermal instability as well as toxicity remain challenging for practical applications [10, 11].

Antimony sulfide, Sb_2S_3, is a low-cost, earth-abundant, non-toxic, and air-stable material, which has attracted much attention recently as a solar cell material [12, 13]. Compared with other metal-chalcogenide PV materials, high-quality Sb_2S_3 films can be synthesized at low temperatures $< 350^{\circ}C$ because it has a relatively low melting point of $550^{\circ}C$ [14]. As for its crystal structure, Sb_2S_3 has a pseudo-one dimensional (1D) structure without dangling bonds or surface states. Therefore, grain boundaries are expected to be electrically benign, incurring a low recombination loss or V_{OC} loss, similar to 1D Sb_2Se_3 [15]. In addition, several studies have also demonstrated that the carrier diffusion length in Sb_2S_3 is on the order of a few hundred nanometers (290-900 nm) [16, 17], longer than the thickness of the Sb_2S_3 layer (80-200 nm) in solar cells

[18] [19] [20]. By engineering the surface defects during the chemical bath deposition of the ultrathin Sb_2S_3 absorber layer, Seok *et al.* obtained 7.5% power conversion efficiency (PCE) in mesoporous sensitized solar cells [19]. A PCE of 6.56% was also achieved in a planar heterojunction solar cell recently [20]. Sb_2S_3 has a bandgap of 1.7-1.8 eV [18, 21-24] and thus can be used as the top cell in a tandem dual-junction solar cell with an expected higher PCE exceeding 40% [25].

By systematically investigating the carrier recombination kinetics, Dennler *et al.* showed that the relatively low PCE of Sb_2S_3 solar cells is related to the large recombination rate in Sb_2S_3 itself, likely caused by the defect-induced subgap states [16]. High resistivity in Sb_2S_3 films (5.0×10^6 and 1.0×10^8 Ω cm for *n*- and *p*-type conductivities, respectively) was observed [18, 26], suggesting the possibility of strong defect compensation. Therefore, a comprehensive understanding of defect properties (especially those of deep traps) and an improved defect management are important for the further optimization of Sb_2S_3 solar cells.

Despite the significant progress made in Sb_2S_3 solar cell recently, the understanding of the defect physics in Sb_2S_3 is still limited [27, 28]. In this paper, hybrid density functional theory calculations are performed to study the electronic structure as well as properties of intrinsic defects, impurities, and defect complexes in Sb_2S_3. Our results show that V_{Sb} and V_S are the dominant defects in Sb_2S_3 and introduce deep states in the band gap. Impurities are investigated for their effects in modifying trap and free carrier densities. Our results show that Zn_{Sb} and Cl_S are much shallower than vacancies (V_{Sb} and V_S) and defect complexes can also effectively make the deep defect levels shallower and less detrimental to carrier transport. Based on our theoretical results, guidelines for further development of Sb_2S_3 based solar cells with improved performance are proposed.

II. Computational methods

Our calculations are based on the Heyd-Scuseria-Ernzerhof (HSE) hybrid functional [29] implemented in the Vienna ab initio simulation package (VASP) [30, 31]. The mixing parameter for the nonlocal Hartree-Fock exchange is set to be 0.25, which yields a band gap of 1.76 eV, which is consistent with experimental indirect band gap of 1.74 eV [22]. The cut off energy for the plane wave basis was set at 400 eV and the atomic positions were fully relaxed until the residual forces are less than 0.01 eV/Å. The Brillouin zone (BZ) integration is sampled by setting a 2 × 8 × 2 Γ-centered *k*-point mesh for the 20-atom primitive cell and a 2 × 2 × 2 Monkhorst-Pack *k*-point mesh for the 1 × 3 × 1 Sb_2S_3 supercell (60 atoms) in the simulation of defect properties. The experimental lattice parameters (a = 11.3107 Å, b = 3.8363 Å, and c = 11.2285 Å [32, 33], space group Pnma) are used in all calculations. Based on our tests using larger supercells, the errors in transition levels are less than 0.1 eV.

The defect formation energy with a charge q is be evaluated by

$$\Delta H_{D,q}(\varepsilon_f, \mu_\alpha) = (E_{D,q} - E_H) - \sum_\alpha n_\alpha (E_\alpha^{ref} + \mu_\alpha) + q(\varepsilon_{\mathrm{VBM}} + \varepsilon_f) \quad , \qquad (1)$$

where $E_{D,q}$ is the total energy of a supercell containing the defect D with a charge q and E_H is the energy of a defect-free cell. n_α represents the number of exchanged atom, E_α^{ref} is the chemical potential of the αth element in its bulk or gas form , and

μ_α is the chemical potential of the αth element referenced to E_α^{ref}. E_{VBM} is the energy of the valence band maximum (VBM) of the host. ε_f is the Fermi level referenced to the VBM. We also applied the image charge correction for charged defects/impurities and the potential alignment correction, which account for the finite-size effects in the supercell calculation of defects [34, 35].

The transition level of a defect, $\varepsilon(q/q')$, corresponding to a change in its charge state between q and q', is given by the Fermi level, at which the formation for charge state q and q' are equals to each other:

$$\varepsilon(q/q') = (\Delta H_{D,q} - \Delta H_{D,q'})/(q'-q) \quad . \tag{2}$$

In order to get stable Sb_2S_3 and avoid the elemental phases of Sb or S under equilibrium growth conditions, the chemical potentials of Sb and S should satisfy the following restriction:

$$\begin{aligned} &\mu_{\mathrm{Sb}} \le 0, \\ &\mu_{\mathrm{S}} \le 0, \\ &2\mu_{\mathrm{Sb}} + 3\mu_{\mathrm{S}} = \Delta H_f(\mathrm{Sb_2S_3}) = -1.07\ \mathrm{eV}\ , \end{aligned} \tag{3}$$

where $\Delta H_f(\mathrm{Sb_2S_3})$ is the heat of formation of Sb_2S_3. At the Sb-rich limit, μ_{Sb} = 0 eV and μ_{S} = -0.357 eV, while at the S-rich limit, μ_{Sb} = -0.535 eV and μ_{S} = 0 eV. The formation energies of Cu, Zn, Cs, Ti, Cl and Br impurities are also considered at above Sb-and S-rich limits.

III. Results and discussion

A. Electronic properties of Sb_2S_3

Sb_2S_3 crystallizes in an orthorhombic structure at room temperature and under atmospheric pressure. The optimized geometry of Sb_2S_3 is shown in Figure 1(a). The 1D Sb_2S_3 chain is along the *b* axis. There are three and two non-equivalent crystallographic sites for S and Sb, respectively. Sb1, S2, and S3 are three-fold coordinated, Sb2 is five-fold coordinated, and S1 is two-fold coordinated. This structure has complex coordination environments with mixed covalent and ionic bond character. Our calculated orbital decomposed density of states (Figure. 1(b)) of Sb_2S_3 shows that the electronic states near the VBM are mainly formed by S 3*p* and Sb 5*s* orbitals, while those near the conduction band minimum (CBM) consist of mainly Sb 5*p* and a small contribution from S 3*p* orbitals. The hybridization between S 3*p* and Sb 5*s* states makes the top valance band more dispersive as demonstrated by the calculated small hole effective mass shown below. The hybrid density functional calculation shows that the band gap of Sb_2S_3 is indirect with value of 1.76 eV [Figure 1(c)], which is consistent well with the experimentally measured values [22, 24] and other calculated results [36, 37]. The band structure of Sb_2S_3 shows that Sb_2S_3 has an indirect band gap with the VBM at Γ point and the CBM located along the Γ-Z line and close to the Z point. Our calculated energy difference of the lowest conduction band between C and Z points is only 3 meV. Our calculated direct band gaps at Γ, C and Z points are 1.98, 1.91 and 1.92 eV, respectively. The calculated optical absorption coefficients of Sb_2S_3 are also shown in Figure 1(d). Note that, the cross-band-gap optical transitions include the efficient onsite transitions between Sb 5*s* and Sb 5*p* levels, which should contribute to the experimentally observed high absorption coefficient [38-40]. Our calculated optical absorption coefficients show that it can achieve 10^4 cm^{-1} at the photon energy of 2.04 eV, which is consistent with the experimental conclusion that absorption coefficients can reach 10^4-10^5 cm^{-1} for photo energies larger than band gap E_g [38-40].

According to our calculated band structure of Sb_2S_3, the top valance band is dispersive along all three crystallographic axes, while the low conduction band is only dispersive along the $\Gamma - Z$ direction (*c* axis) close to CBM and the $\Gamma - X$ direction (*b* axis); the low conduction band along the $\Gamma - Y$ direction (*a* axis) is very flat, indicating anisotropic electron transport. In Sb_2S_3, our calculated average effective mass of hole is 0.17 m_0 around VBM ($m_h^{\Gamma-X}$ = 0.11 m_0, $m_h^{\Gamma-Z}$ = 0.20 m_0, $m_h^{\Gamma-Y}$ = 0.21 m_0), which is smaller than the average effective mass of electron 0.28 m_0 around CBM ($m_e^{C-\Gamma}$ = 0.25 m_0, m_e^{C-Z} = 0.30 m_0, here C donates the *k* point where CBM locates). The small hole effective masses are comparable to those in other good solar absorber materials such as Si (0.19 m_0) [41], CdTe (0.11 m_0) [42], $CuZnSnS_2$ (0.23 m_0) [41] and $MAPbI_3$ (0.28 m_0) [43]. Thus, Sb_2S_3 can be an excellent hole transport material in a thin-film solar cell.

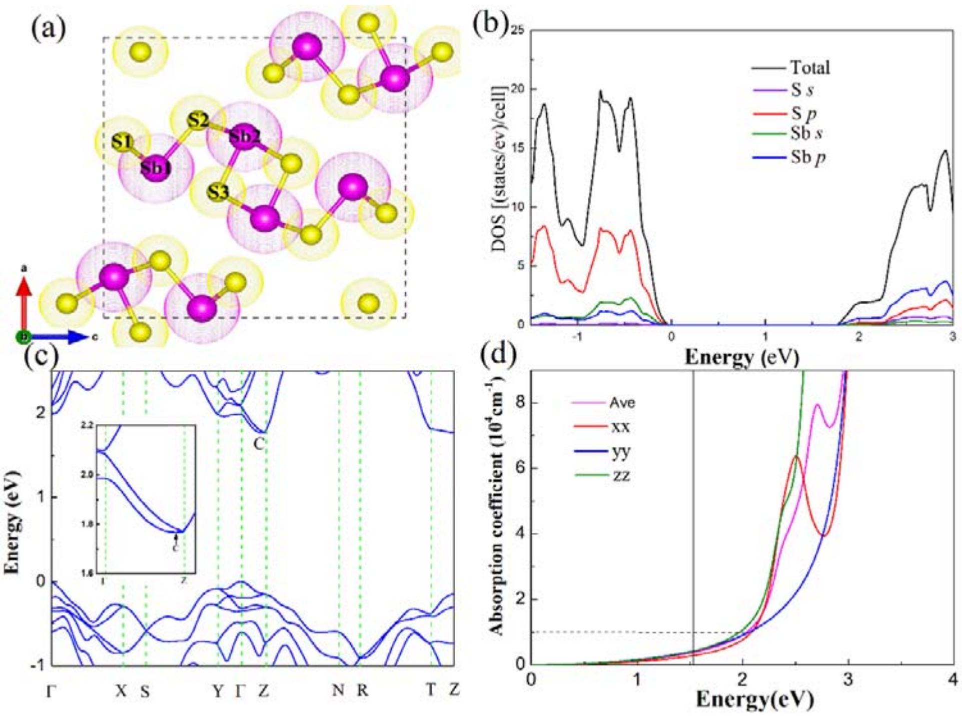

Figure 1. (a) The crystal structure of 20-atom Sb_2S_3 unit cell with yellow and purple balls representing S anions Sb cations, respectively, (b) Partial density of states (DOS), (c) band structure, and (d) Optical absorption coefficients of Sb_2S_3.The inset at (c) shows the conduction band near the CBM (the C point).

B. Native point defects in Sb_2S_3

There are three and two nonequivalent crystallographic sites for S and Sb, respectively. We consider point defects on all nonequivalent sites as shown in Figure 1(a), *i.e.*, (i) sulfur vacancy (V_{S1}, V_{S2}, V_{S3}), (ii) cation vacancy (V_{Sb1} and V_{Sb2}), (iii) the anion-replace-cation antisite (S_{Sb1} and S_{Sb2}), (IV) cation-replace-anion antisite (Sb_{S1}, Sb_{S2} and Sb_{S3}), (V) S interstitial (S_i), (VI) Sb interstitial (Sb_i) .

Formation energies of all defects as a function of the Fermi level under both Sb- and S-rich conditions are shown in Figure 2. As can be seen, the most important native defects in Sb_2S_3 are vacancies, *i.e.*, V_{Sb}, acting as an acceptor, and V_S, acting as a donor. The defects with low formation energies should play dominate roles in transport properties. In the absence of a high concentration of impurities, the Fermi level should be close to the crossing point of the formation energy lines for the lowest-energy native donor and acceptor defects. For both S and Sb rich conditions, the Fermi level is close to midgap ($\varepsilon_{\mathrm{VBM}}$ + 0.85 eV and $\varepsilon_{\mathrm{VBM}}$ + 1.03 eV, respectively, crossing point of formation energy lines of V_{S2} and V_{Sb1}) , which is consistent with the measured high resistivity of 1.0×10^8 or 5.0×10^6 Ω cm in Sb_2S_3 thin films with *p*- or *n*-type conductivity [18, 26].

V_S is the main donor defect in Sb_2S_3 under both S- and Sb-rich conditions, which accords well with the common phenomenon that the anion vacancy is usually a low-energy donor defect in compound semiconductors [44]. The formation energies of V_S on the three S sites are slightly different. V_{S2} is the most stable followed by V_{S1} and V_{S3}. Interestingly, V_{S2} is a shallow donor while V_{S1} and V_{S3} are both deep donors. The transition level $\varepsilon(0/2+)$ for V_{S1} and V_{S3} are located at 1.18 and 1.00 eV above the VBM, respectively. The shallow nature of V_{S2} is likely related to the relatively long Sb-Sb distance around V_{S2}. In defect-free Sb_2S_3, the average Sb-Sb distances around S1, S2, S3 are 3.84 Å, 3.95 Å, and 3.88 Å, respectively. For 2+ charged V_{S1}, V_{S2}, and V_{S3}, the average Sb-Sb distances around the vacancy are increased to 4.20, 4.53 and 4.19 Å, respectively, due to the Coulomb repulsion. The neighboring Sb atoms around the S vacancy are able to move toward the center of the vacancy to enhance the Sb-Sb hybridization and trap two electrons, forming neutral V_{S1} and V_{S3}. Such deep electron trapping and the associated structural relaxation are energetically unfavorable for V_{S2} as a result of the long Sb-Sb distance; thus, only shallow trapping at a hydrogenic level is possible.

Sb vacancies (V_{Sb}) are also dominant defects in Sb_2S_3. Figure 2 shows that, between the two Sb sites, V_{Sb1} is more stable and both V_{Sb1} and V_{Sb2} introduce deep hole trapping levels, which are detrimental to hole transport efficiency. Compared with V_S and V_{Sb}, antisites S_{Sb} and Sb_S have higher formation energies under both Sb-and S-rich growth conditions. For the cation interstitial (Sb_i) or anion interstitial (S_i) in Sb_2S_3, six different interstitial sites are constructed. Sb_i and S_i donor defects possess deep transition levels, which can act as charge recombination centers. However, their formation energies are high at the Fermi pinning level, indicating that their effect on conductivity should be minimal. Note that in Sb_2Se_3 [45, 46], except vacancies V_{Sb} and V_{Se}, antisites Sb_{Se} and Se_{Sb} can also be the lowest-energy defects possibly due to the small size difference between Sb and Se. The high formation energies of antisite defects in Sb_2S_3 is likely due to the larger size difference between Sb and S, and this trend is more obviously in Bi_2S_3 [47]. This atomic size difference between Bi, Sb and Se, Se and Te have significant influence on the properties of antisite defects like formation energy and transition level.

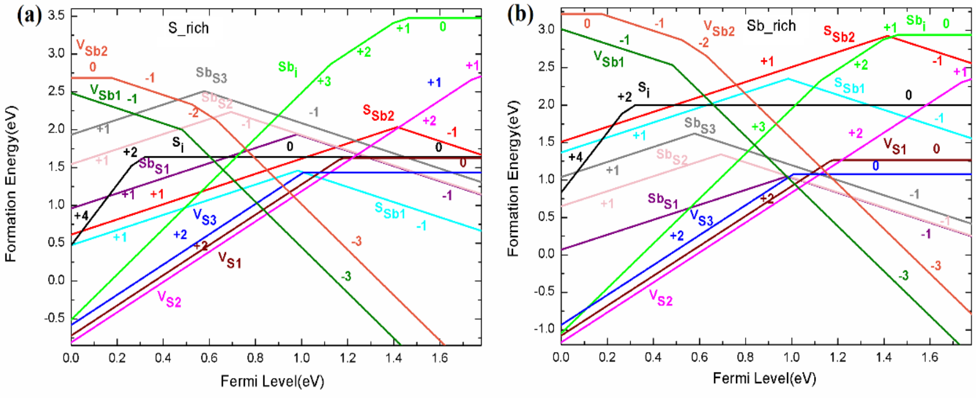

Figure 2. Calculated intrinsic defect formation energies in Sb_2S_3 under (a) S- and (b) Sb-rich conditions. A transition level is where the slope of a formation energy line changes.

Figure 3 presents our calculated transition energy levels of the above native defects in Sb_2S_3. Our results show that all defects except V_{S2} introduce deep traps. Deep level transient spectroscopy (DLTS) is a powerful technique to characterize the properties of defects [48-50]. Several DLTS measurements have been performed for Sb_2Se_3 and $Sb_2(S,Se)_3$ alloys, while for pristine Sb_2S_3 there are only a few reports. One deep acceptor level (H1) at 0.52 eV above the VBM was observed in Sb_2S_3 by DLTS [51]. On the other hand, three hole traps (H1, H2, H3) located at 0.507, 0.689 and 0.762 eV above the VBM were observed in $Sb_2(S_{1-x}Se_x)_3$ with x=0 and x=0.17. Increasing the Se concentration to x = 0.29 (0.48), only two hole traps at 0.502 and 0.766 (0.490 and 0.768) eV were found [52]. The different hole trapping levels reported in Refs. 51 and 52 may be related to different growth environments. Wen *et. al.* observed the two hole traps located at 0.48 ± 0.07 (0.49 ± 0.03) and 0.71 ± 0.02 (0.74 ± 0.04) eV above VBM and one electron trap at 0.61 ± 0.03 (0.60 ± 0.02) eV below the CBM in Sb_2Se_3 sample processed by vapor transport deposition (rapid thermal evaporation) method [53]. Ma *et. al.* also found two hole traps at Ev + 0.48 eV and Ev + 0.71 eV and one electron trap level (E1) at Ec - 0.63 eV in Sb_2Se_3; these trap levels remains nearly the same after doping by 5.23% S [54]. The two hole traps were attributed to V_{Sb} and Sb_{Se}, respectively, and the electron trap was assigned to Se_{Sb} [53]. For comparison, our calculated hole trapping levels of (-/2-) for V_{Sb1}, (-/2-)

for V_{Sb2}, and (2-/3-) for V_{Sb2} in Sb_2S_3 are 0.75, 0.52, and 0.63 eV, respectively, which are in good agreement with those measured by DLTS [52]. In addition, our calculated (0/-) levels for Sb_{S1}, Sb_{S2}, and Sb_{S3},which are 0.48, 0.45 and 0.47 eV above the VBM, respectively, are also very close to those measured by DLTS [52]. Thus, both V_{Sb} and Sb_S may account for the observed hole traps in DLTS measurements. Note that Sb_S is a negative-U center; neutral Sb_S is metastable and thus the (0/-) levels of Sb_S are not shown in Figures 2 and 3 (see all the transition levels of vacancies and antisites for Sb_2S_3 in the Supplemental Material [55]). Only the stable charge states of +1 and -1 for Sb_S are shown in Figures 2 and 3. The (0/-) level is a single-hole trapping level, which is compared with the DLTS-observed hole trapping levels as discussed above. For the negative U defect, the conventional DLTS transient is determined by the first slower emission process, another faster emission follows immediately. If biased injection is replaced by the optical injection, both of the emission processes can be observed. Considering the thermal barrier associated with the transition level, the slower emission corresponds to the transition with deeper level reference to CBM or VBM.

Next, we investigate impurities and their complexes with native defects for their potential effects on trap levels and densities.

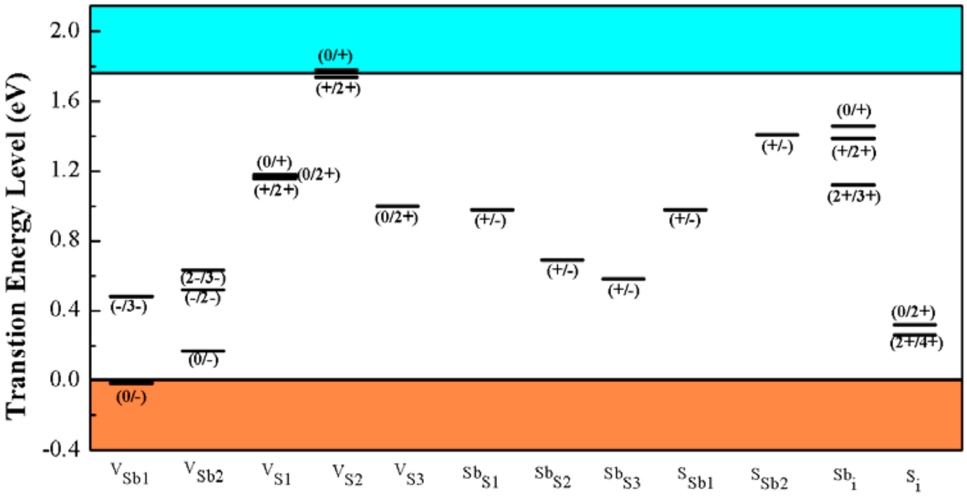

Figure 3. Transition energy levels of intrinsic defects on different atomic sites in the band gap of Sb_2S_3.

C. Impurities and defect complexes in Sb_2S_3

The above results show that an intrinsic Sb_2S_3 film should have high resistivity with *p*- or *n*-type conductivity under S-rich and Sb-rich conditions, respectively. In most of Sb_2S_3 solar cells, Sb_2S_3 shows *n*-type conductivity [20]. To control the carrier transport in Sb_2S_3, extrinsic dopants (including Zn, Cu, Ti, Br and Cl) and their complexes with native defects are investigated.

Zn_{Sb} and Cu_{Sb} both act as acceptors; the former is shallow while the latter is deep. The formation energies of Zn_{Sb} and Cu_{Sb} together with V_{Sb} and V_S are showed in Figure 4 under both Sb- and S-rich conditions. Compared to undoped Sb_2S_3, the Fermi level is lower in energy close to the crossing point of formation energies line of Zn_{Sb} (Cu_{Sb}) acceptor and V_S donor, resulting in higher hole density. For example, under the S-rich condition the crossing point determined by Zn_{Sb1} (Cu_{Sb1}) and V_{S2} locates at 0.56 (0.57) eV above the VBM, lower than that of 0.85 eV in undoped

Sb_2S_3. A lower Fermi level suppresses the formation of V_{Sb} deep acceptors but increases the density of V_S donor defects. For the deep acceptor Cu_{Sb}, the (-/2-) transition levels of Cu_{Sb1} and Cu_{Sb2} are 0.70 and 0.50 eV above VBM, respectively, as shown in Figure 5.

For *n*-type doping, our results show that Ti_{Sb} is a donor with deep (0/+) ionization energy levels of 0.55 and 0.61 eV below the CBM for the Sb1 and Sb2 sites, respectively. On the other hand, both Cl_S and Br_S have shallow donor levels. Because the size difference between Cl and S is smaller than that between Br and S, the formation energy of Cl_S is lower than that of Br_S (only results of Cl are present in Figure 4). The (0/+) transition levels for Cl_{S1} and Cl_{S3} are 0.04 and 0.09 eV below the CBM, respectively, while for Cl_{S2} is somewhat deep at 0.15 eV. For Br_{S1}, the (0/+) transition level is 0.03 eV, while for Br_{S2} and Br_{S3}, the transition levels are 0.18 and 0.24 eV, respectively. Cl doping can raise the Fermi level, for example, under the Sb-rich conduction, the Cl-doped Sb_2S_3 has the Fermi level close to 1.19 eV above the VBM (determined by V_{Sb1} and Cl_{S1}) as shown in Figure 4, higher than that of 1.03 eV above the VBM (determined by V_{Sb1} and V_{S2}) in undoped Sb_2S_3.

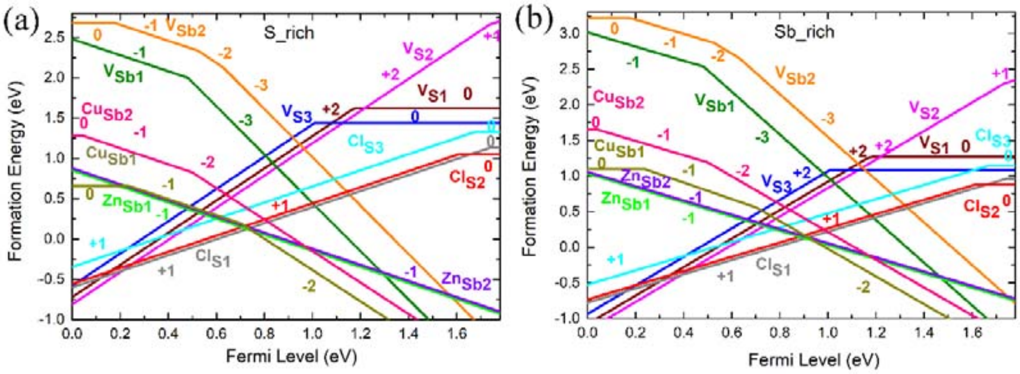

Figure 4. Calculated the dopant formation energies in Sb_2S_3 under S-rich and Sb-rich

growth conditions. A transition level is where the slope changes.

Dopants can bind with native defects, forming defect complexes, and modify the defect level position. The dopant-defect coupling can potentially make a defect shallower [56]. Here we mainly focus on some chosen donor-acceptor complexes, such as Cu_{Sb}+V_S, Zn_{Sb}+V_S, and Cl_S+V_{Sb}. In these complexes, the dopant and the defect are chosen to be nearest neighbors for enhancing their coupling strength. The goal is to make the deep V_S and V_{Sb} defects shallower, *i.e.*, less harmful to carriers transport. The fully passivated complexes $2Zn_{Sb}$+V_S and $3Cl_S$+V_{Sb} are also studied.

Cu_{Sb} acceptor can easily bind with a V_S donor, forming a neutral Cu_{Sb}+V_S complex. The electrons of V_S transfer to the Cu_{Sb}. Our calculated (-/0) and (0/+) transition levels of Cu_{Sb1}+V_{S1} are located at 0.04 below the CBM and 0.16 eV above the VBM, respectively, which are shallower than the (2+/+) electron-trapping level of $(V_{S1})^+$ and the (2-/-) hole-trapping level of $(Cu_{Sb1})^-$. These levels are much shallower than those of the isolated defects because the donor-acceptor coupling pushes the electron and hole-trapping levels away from each other. As a result, the electronic trapping level is closer to the CBM and the hole-trapping level is closer to the VBM, as shown in Figure 5. To demonstrate this more clearly, the charge densities are also plotted in Figure 6. As we can see, the charge densities of isolated V_{S1} and Cu_{Sb1} are localized around the S vacancy and Cu_{Sb1}, respectively, while the charge density of the Cu_{Sb1}+V_{S1} complex are much more delocalized, which accord well with the deep and shallower levels we obtained. Furthermore, Cu_{Sb1}+V_{S1} has a binding energy -0.72 eV, which indicates that the complexes are not easy to dissociate once they are formed under growth conditions. As for the most stable Cu_{Sb}-V_S complex, *i.e.*, Cu_{Sb2}+V_{S3}, its defect levels also become shallower than those of the isolated defects. Their (0/-) and (0/+) transition levels are E_{CBM} - 0.08 eV and E_{VBM} + 0.39 eV, which are shallower than the (0/2+) transition level of V_{S3} and the (-/-2) transition level of Cu_{Sb2}, which are E_{CBM} - 0.76 and E_{VBM} + 0.50 eV, respectively. For complexes Cu_{Sb1}+V_{S2} and Cu_{Sb2}+V_{S2}, since isolated V_{S2} itself is shallow donor, the coupling between a delocalized donor level and a localized acceptor level is not as strong as between two localized levels. The (0/+) levels of Cu_{Sb1}+V_{S2} and Cu_{Sb2}+V_{S2} are a little deeper than those of Cu_{Sb1}+V_{S1} and Cu_{Sb2}+V_{S3}.

A V_S donor can also bind with a Zn_{Sb} acceptor, resulting in a Zn_{Sb}+V_S complex. For the (0/+) transition level of Zn_{Sb1}+V_{S1} is at 0.53 eV below CBM, similar to the (+/2+) level of V_{S1} at 0.60 eV below the CBM. For Zn_{Sb1}+V_{S2} and Zn_{Sb2}+V_{S2}, their (0/+) levels are at 0.09 and 0.18 eV below the CBM, respectively, relatively deeper than the (+/2+) level of V_{S2} at 0.02 eV below the CBM, due to the structure distortion introduced by the substitution of Sb by Zn in the complex. For Zn_{Sb2}+V_{S3}, its (0/+) level is at 0.29 eV below the CBM, much shallower than the (0/2+) level of V_{S3} at 0.76 eV below the CBM, while similar to the (+/2+) level of V_{S3} at 0.30 eV below the CBM (this level is unstable and not shown in Figures 3 and 5). Our above results demonstrate that the delocalization character of Zn_{Sb} leads to the weak interaction between Zn_{Sb} and V_S in partially passivated complex Zn_{Sb}+V_S. The fully passivated complex $2Zn_{Sb1}$+V_{S1} is also studied and no localized states is found.

Donor defect Cl_S, can also bind to the acceptor defect V_{Sb}, forming complexes

Cl_S+V_{Sb}. For Cl_{S3}+V_{Sb2}, the (-/2-) level at 0.26 eV is much shallower than the (2-/3-) level of V_{Sb2} at 0.63 eV, and for Cl_{S2}+V_{Sb1}, the (-/2-) level at 0.17 eV is also shallower than the (-/3-) level of V_{Sb1} at 0.48 eV (unstable (2-/3-) level of V_{Sb1} at 0.21 eV). For the fully passivated complex 3Cl_S+$V_{Sb1,}$ the (0/+) and (0/-) levels are 0.04 and 0.08 eV, respectively, which are less harmful to the carrier transport.

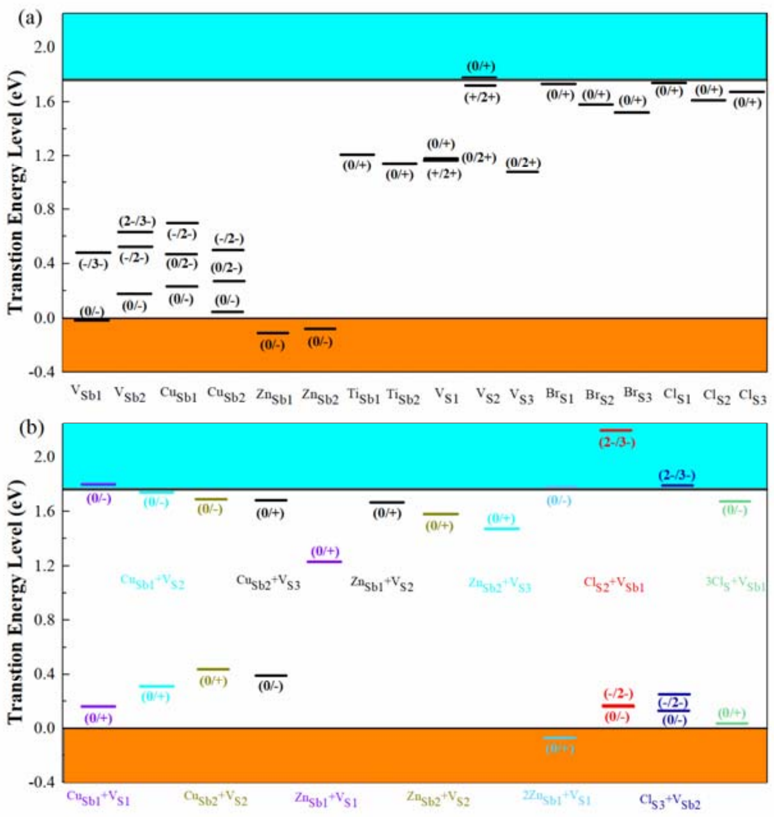

Figure 5. The transition levels of different impurities and defect complexes in Sb_2S_3.

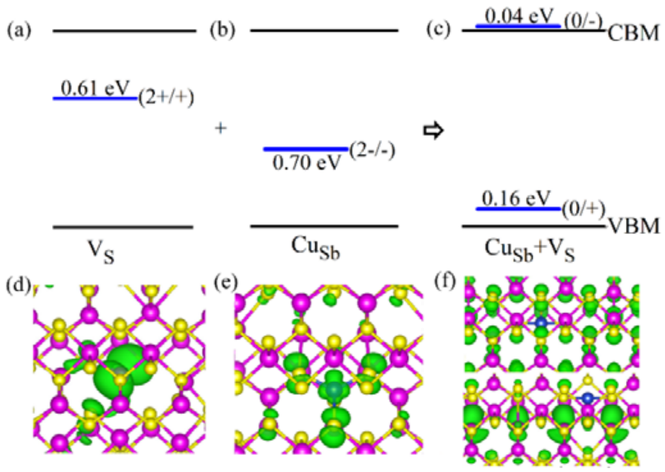

Figure 6. Effects of Cu$_{Sb1}$-V$_{S1}$ binding on the electron trapping level of V$_{S1}$ and the hole trapping level of Cu$_{Sb1}$.(a) and (d) show the (2+/+) electron trapping level of V$_{S1}$ and the charge density of the trapped electron at $(V_{S1})^+$, respectively; (b) and (e) show the (2-/-) hole trapping level of Cu$_{Sb1}$ and the charge density of the trapped hole at $(Cu_{Sb1})^-$, respectively; (c) shows the (0/-) electron trapping and the (+/0) hole trapping levels of Cu$_{Sb1}$+V$_{S1}$ and (f) shows the trapped electron at $(Cu_{Sb1}+V_{S1})^-$ (upper panel) and the trapped hole at $(Cu_{Sb1}+V_{S1})^+$ (lower panel).

When two defects bind to form a defect complex, the formation energy may be lowered through interactions like charge compensation, subsequent Coulomb attraction and atomic relaxation driven by strain relief [56]. Therefore, the position of Fermi level pinned by donor and acceptor defects with lowest formation energies may be changed after considering the effect of defect complexes. Figure 7 plot the formation energies of different defect complexes along with native defects studied above. For Cu doping showed in Figure 7 (a) and (b), in the case of S rich, the Fermi level is close to 0.57 eV above the VBM determined by V$_{S2}$ and Cu$_{Sb1}$. For Zn doping, in the case of S rich, the Fermi level is close to 0.65 eV above VBM determined by

Zn_{Sb1} and complex $Zn_{Sb1}+V_{S2}$. For Cl doping, in the case of Sb rich, the Fermi level is close to 1.10 eV above the VBM determined by Cl_{S1} and complex $Cl_{S2}+V_{Sb1}$. Therefore, compared with the Fermi level pinned by point defects, the Fermi level does not change much.

Our above results show that donor (such as Cl) and acceptor (such as Zn or Cu) doping can increase carrier density by moving the Fermi level and reduce the trapping energies at defects by forming complexes with native defects, leading to improved solar cell performance.

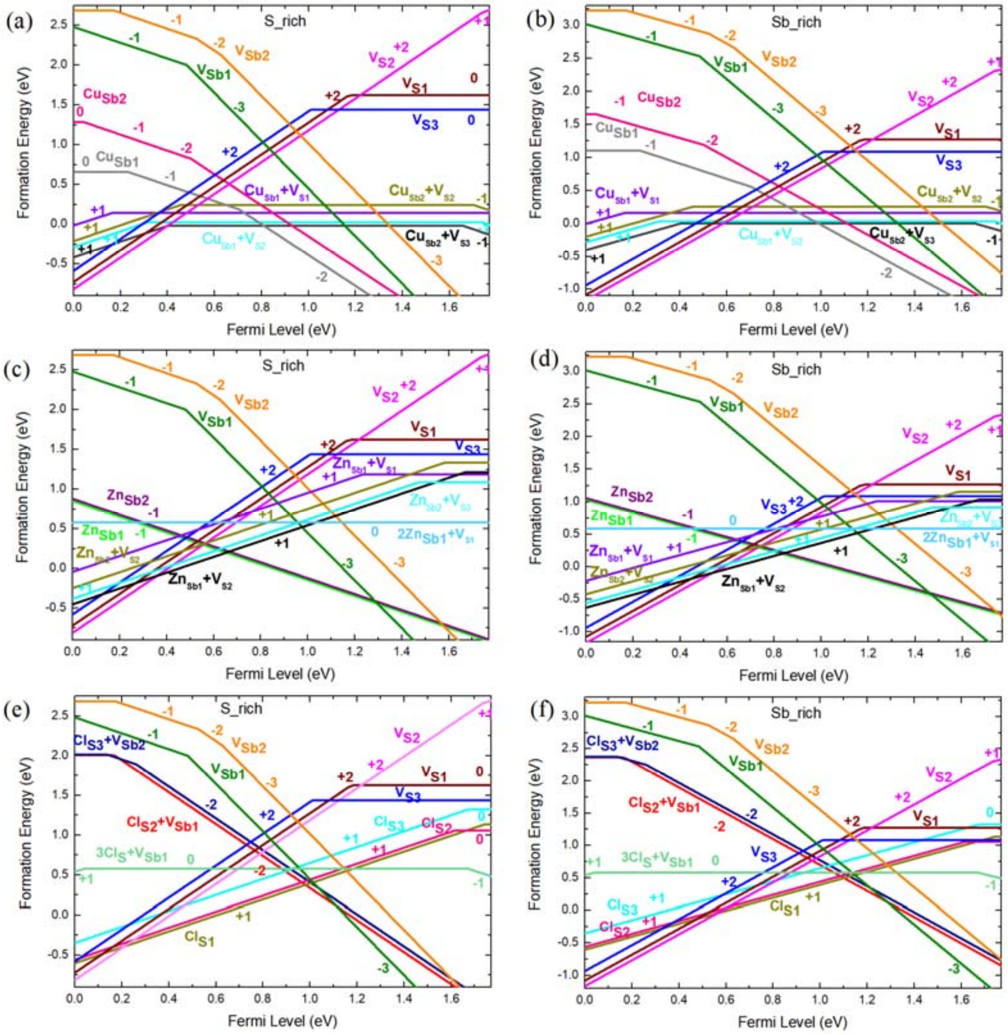

Figure 7. Calculated formation energies of different defect complexes in Sb_2S_3 under

S-rich and Sb-rich growth conditions. A transition level is the Fermi level where the slope of a formation energy line changes.

D. Band alignment with other materials

As shown in Figure 8, the experimental band offset versus vacuum between different semiconductor materials used in solar cells is presented. Electrons from Sb_2S_3 [57] or Sb_2Se_3 [58] can be injected to ZnO [59], TiO_2 [57] or CdS [60], while holes are blocked. As shown above, chemical doping in Sb_2S_3 can modify the Fermi level and consequently changes the charge transfer and band offset at the interface with the electron-extracting layer, providing additional means to tune the charge separation and transport efficiencies. A Sb_2S_3 cell may also be coupled with a Si or Sb_2Se_3 cell to form a multi-junction tandem cell. Considering the small hole effective mass and the intrinsically benign grain boundaries of Sb_2S_3, *p*-type Sb_2S_3 may also be used as a hole transport material in solar cells.

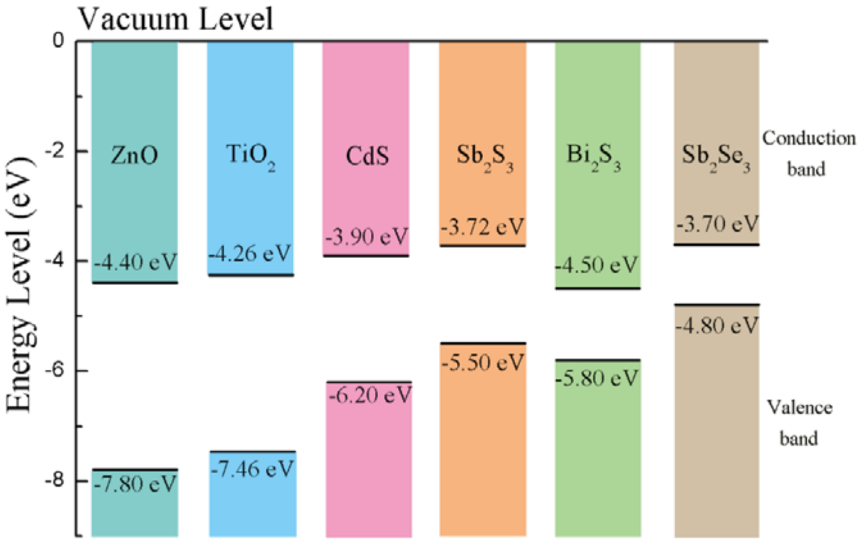

Figure 8. The experimental energy level of band edge versus vacuum of different photovoltaic semiconductor materials [57-60].

IV. Conclusion

In summary, electronic structure, native defects, dopants, and dopant-defect complexes in Sb_2S_3 are studied by hybrid density functional theory calculations. The calculated small hole effective masses and strong optical absorption are favorable for photovoltaic applications. S and Sb vacancies are the dominate donor and acceptor defects with low formation energies in Sb_2S_3 and both introduce deep trapping levels, which are detrimental to carrier transport. We identified signals of deep level transient spectroscopy for hole traps to vacancy Sb and antisite Sb_S. Chemical doping by shallow donors (e.g., Cl, Br) or shallow acceptors (e.g., Zn) can modify the Fermi level, resulting in a higher carrier density and providing means to fine tune the properties of the interface with other components of the solar cell (such as the electron-extraction layer and the hole-transport layer). By complexing with native defects, Cl/Br and Zn dopants can also reduce the trapping energy of the native defects, improving the carrier transport efficiency. We hope that this work can serve as a useful guide to designing higher efficiency Sb_2S_3 photovoltaic devices.

Acknowledgements

H. Shi was supported by the National Natural Science Foundation of China (NSFC) under Grants No.11604007 and the start-up funding at Beihang University. The work at ORNL were supported by the U. S. Department of Energy, Office of Science, Basic Energy Sciences, Materials Sciences and Engineering Division.

References

[1] A. W. Blakers, A. Wang, A. M. Milne, J. Zhao, and M. A. Green, Appl. Phys. Lett. 55, 1363 (1989).

[2] J. M. Burst, and A. Petrozza, Nat. Energy **1**, 16015 (2016).

[3] P. Jackson, D. Hariskos, E. Lotter, S. Paetel, R. Wuerz, R. Menner, W. Wischmann, and M. Powalla, Prog. Photovolt: Res. Appl. **19**, 894 (2011).

[4] A. Polizzotti, I. L. Repins, R. Noufi, S. Wei, and D. B. Mitzi, Energ. Environ. Sci. **6**, 3171 (2013).

[5] W. S. Yang, J. H. Noh, N. J. Jeon, Y. C. Kim, S. Ryu, J. Seo, and S. I. Seok, Science **348**, 1234 (2015).

[6] A. D. Compaan, Sol. Energ. Mat. Sol. C. **90**, 2170 (2006).

[7] V. Avrutin, N. Izyumskaya, and H. Morkoç, Superlattic Microst. **49**, 337 (2011).

[8] J. D. Beach, and B. E. McCandless, Mrs. Bull. **32**, 225 (2007).

[9] S. B. Zhang, S. H. Wei, A. Zunger, and H. Katayama-Yoshida, Phys. Rev. B **57**, 9642 (1998).

[10] A. H. Slavney, R. W. Smaha, I. C. Smith, A. Jaffe, D. Umeyama, and H. I. Karunadasa, Inorg. Chem. **56**, 46 (2016).

[11] M. Grätzel, Nat. Mater. **13**, 838 (2014).

[12] S. Moon, Y. Itzhaik, J. Yum, S. M. Zakeeruddin, G. Hodes, and M. Grätzel, J. Phys. Chem. Lett. **1**, 1524 (2010).

[13] J. Han, S. J. Wang, J. B. Yang, S. H. Guo, Q. Cao, H. J. Tang, X. Y. Pu, B. Y. Gao, and X. H. Li, Acs. Appl. Mater. Inter. **12**, 4970 (2020).

[14] Y. Jiang, T. Cao, Y. Shi, and N. Cai, Ecs. Transactions **91**, 2001 (2019).

[15] Y. Zhou, L. Wang, S. Y. Chen, S. K. Qin, X. S. Liu, J. Chen, D. J. Xue, M. Luo, Y. Z. Cao, and Y. B. Cheng, Nat. Photonics **9**, 409 (2015).

[16] A. Darga, D. Mencaraglia, C. Longeaud, T. J. Savenije, B. O Regan, S. Bourdais, T. Muto, B. Delatouche, and G. Dennler, J. Phys. Chem. C **117**, 20525 (2013).

[17] T. Englman, E. Terkieltaub, and L. Etgar, J. Phys. Chem. C **119**, 12904 (2015).

[18] M. I. Medina-Montes, Z. Montiel-González, F. Paraguay-Delgado, N. R. Mathews, and X. Mathew, J. Mater. Sci-Mater. El. **27**, 9710 (2016).

[19] Y. C. Choi, T. N. Mandal, W. S. Yang, Y. H. Lee, S. H. Im, J. H. Noh, and S. I. Seok, Angew. Chem. Int. Edit. **53**, 1329 (2014).

[20] H. Lei, J. Chen, Z. Tan, and G. Fang, Solar RRL **3**, 1900026 (2019).

[21] Z. S. El Mandouh, and S. N. Salama, J. Mater. Sci. **25**, 1715 (1990).

[22] O. Savadogo, and K. C. Mandal, J. Electrochem. Soc. **139**, L16 (1992).

[23] C. Ghosh, and B. P. Varma, Thin Solid Films **60**, 61 (1979).

[24] I. K. E. Zawawi, A. Abdel-Moez, F. S. Terra, and M. Mounir, Thin Solid Films **324**, 300 (1998).

[25] A. De Vos, J. Phys. D: Appl. Phys. **13**, 839 (1980).

[26] O. Savadogo, and K. C. Mandal, Appl. Phys. Lett. **63**, 228 (1993).

[27] Z. H. Cai, and S. Y. Chen, J Appl. Phys. **127**, 183101 (2020).

[28] Z. H. Cai, C. M. Dai, and S. Y. Chen, Solar RRL **4,** 1900503 (2019).

[29] J. Heyd, G. E. Scuseria, and M. Ernzerhof, J. Chem. Phys. **118**, 8207 (2003).

[30] G. Kresse, and J. Furthmüller, Phys. Rev. B **54**, 11169 (1996).

[31] G. Kresse, and J. Hafner, Phys. Rev. B **47**, 558 (1993).

[32] A. Kyono, M. Kimata, M. Matsuhisa, Y. Miyashita, and K. Okamoto, Phys. Chem. Miner. **29**, 254

(2002).

[33] A. Kyono, and M. Kimata, Am. Mineral. **89**, 932 (2004).

[34] S. Lany, and A. Zunger, Phys. Rev. B **78**, 235104 (2008).

[35] C. G. Van de Walle, and J. Neugebauer, J. Appl. Phys. **95**, 3851 (2004).

[36] T. Fujita, K. Kurita, K. Takiyama, and T. Oda, J. Phys. Soc. Jpn. **56**, 3734 (1987).

[37] R. Kondrotas, C. Chen, and J. Tang, Joule **2**, 857 (2018).

[38] A. M. Salem, and M. S. Selim, J. Phys. D: Appl. Phys. **34**, 12 (2001).

[39] F. Aousgi, and M. Kanzari, Curr. Appl. Phys. **13**, 262 (2013).

[40] J. Escorcia-García, D. Becerra, M. Nair, and P. K. Nair, Thin Solid Films **569**, 28 (2014).

[41] J. Feng, and B. Xiao, J. Phys. Chem. Lett **5**, 1278 (2014).

[42] L. D. Whalley, J. M. Frost, B. J. Morgan, and A. Walsh, Phys. Rev. B **99**, 85207 (2019).

[43] K. Galkowski, A. Mitioglu, A.Miyata, P. Plochocka, O. Portugall, G. E. Eperon, J. T. W. Wang, T. Stergiopoulos, S. D. Stranks, Samuel D, H. J. Snaith, Energ. Environ. Sci. **9**, 962 (2016).

[44] J. M. Ball, and A. Petrozza, Nat. Energy **1**, 16149 (2016).

[45] C. N. Savory, and D. O. Scanlon, J. Mater. Chem. A **7**, 10739 (2019).

[46] M. Huang, P. Xu, D. Han, J. Tang, and S. Chen, Acs. Appl. Mater. Inter. **11**, 15564 (2019).

[47] D. Han M. H. Du, C. M. Dai, D. Y. Sun, and S. Y. Chen, J. Mater. Chem. A **5,** 6200 (2017).

[48] D. Wickramaratne*,* C. E. Dreyer, B. Monserrat, J. X. Shen, J. L. Lyons, and A. Alkauskas, Appl. Phys. Lett. **113,** 192106 (2018).

[49] A. R. Peaker, V. P. Markevich, and J. Coutinho, J. Appl. Phys. **123**, 161559 (2018).

[50] D. V. Lang, J. Appl. Phys. **45**, 3023 (1974).

[51] Y. C. Choi, D. U. Lee, J. H. Noh, E. K. Kim, and S. I. Seok, Adv. Funct. Mater. **24**, 3587 (2014).

[52] R. F. Tang, X. M. Wang, W. T. Lian, J. L. Huang, Q. Wei, M. L. Huang, Y. W. Yin, C. H. Jiang, S. F. Yang, G. H. Xing, S. Y. Chen, C. F. Zhu, X. J. Hao, M. A. Green, T. Chen, Nat. Energy, **5,** 587 (2020).

[53] X. X. Wen, C. Chen, S. C. Lu, K. H. Li, R. Kondrotas, Y. Zhao, W. H. Chen, L. Gao, C. Wang, J. Zhang, G. D. Niu, J. Tang, Nat. Commun. **2**, 2179 (2018).

[54] Y. Y. Ma, B. B. Tang, W. T. Lian, C. Y. Wu, X. M. Wang, H. X. Ju, C. F. Zhu, F. J. Fan, T. Chen, J. Mater. Chem. A, **8,** 6510 (2020).

[55] See Supplemental Material at www for all the transition levels of vacancies and antisites for Sb_2S_3.

[56] S. B. Zhang, S. H. Wei, A. Zunger, and H. Katayama-Yoshida, Phys. Rev. B **57,** 9642 (1998).

[57] X. Jin, Y. Yuan, C. Jiang, H. Ju, G. Jiang, W. Liu, C. Zhu, and T. Chen, Sol. Energ. Mat. Sol. C **185**, 542 (2018).

[58] Y. Zhang, J. Li, G. Jiang, W. Liu, S. Yang, C. Zhu, and T. Chen, Solar RRL **1**, 1700017 (2017).

[59] K. Takanezawa, K. Tajima, and K. Hashimoto, Appl. Phys. Lett. **93**, 297 (2008).

[60] X. Wang, R. Tang, Y. Yin, H. Ju, C. Zhu, and T. Chen, Sol. Energ. Mat. Sol. C **189**, 5 (2019).